Geochemistry Geophysics Geosystems G3
AN ELECTRONIC JOURNAL OF THE EARTH SCIENCES
Published by AGU and the Geochemical Society

Article
Volume 8, Number 10
13 October 2007
Q10004, doi:10.1029/2007GC001661
ISSN: 1525-2027

Click Here for Full Article

Ubiquitous low-velocity layer atop the 410-km discontinuity in the northern Rocky Mountains

John Jasbinsek and Kenneth Dueker

Department of Geology and Geophysics, University of Wyoming, 1000 East University Avenue, Department 3006, Laramie, Wyoming 82071, USA (johnjj@uwyo.edu)

[1] Receiver functions from three 30-station IRIS-PASSCAL small-aperture arrays (2–15 km station spacing) operated for 10 months each in the northern Rocky Mountains show a ubiquitous negative polarity P to S conversion just preceding the 410-km discontinuity arrival. Data from the three arrays were sorted into NW, SE, and SW back-azimuth quadrants and stacked to form nine quadrant stacks. Remarkably, the negative polarity arrival (NPA) is apparent in 8 of the 9 quadrant stacks, with 7 of the 8 having well-correlated waveforms. Each quadrant stack also contains clear P to S conversions from the 410- and 660-km discontinuities. Moveout analysis shows that all the major phases display the correct moveout for forward scattered P-S phases. The waveshapes for the seven similar NPA-410 km discontinuity arrivals are modeled with a five-parameter "double gradient slab" model that is parameterized as follows: a top gradient thickness and shear velocity decrease; a constant velocity layer; bottom gradient thickness; and shear velocity increase. Model misfit is assessed via a grid search over the model space using a reflectivity code to calculate synthetic seismograms. Model likelihood is determined by calculating 1- and 2-D marginal probability density functions (PDF) for the five parameters. The 1-D marginals display a range of peak values, although significant overlap is observed for the top gradient thickness and its associated velocity decrement. From the peak value of the summary PDF, we find the top velocity gradient to be sharp (<6.4 km) and the shear velocity decrement to be large (8.9% V_S). Defining an effective thickness of the low-velocity layer as the mean layer thickness plus half the mean gradient thicknesses, the 410 low-velocity layer thickness is found to be 22 km. A review of changes in the physical state required to match our new 410-LVL constraints suggests that the water-filter model remains an operative hypothesis to test.

Components: 7816 words, 16 figures, 3 tables.

Keywords: 410-km discontinuity.

Index Terms: 7208 Seismology: Mantle (1212, 1213, 8124); 7203 Seismology: Body waves; 1038 Geochemistry: Mantle processes (3621).

Received 17 April 2007; **Revised** 18 July 2007; **Accepted** 14 August 2007; **Published** 13 October 2007.

Jasbinsek, J., and K. Dueker (2007), Ubiquitous low-velocity layer atop the 410-km discontinuity in the northern Rocky Mountains, *Geochem. Geophys. Geosyst.*, *8*, Q10004, doi:10.1029/2007GC001661.

1. Introduction

[2] A provocative new model, the "transition zone water filter," predicts that a spatially localized layer of melt may pool atop the 410-km discontinuity (d410) resulting from the difference in water solubility between the mantle transition zone and overlying upper mantle [*Bercovici and Karato*,

2003]. If the transition zone is sufficiently hydrated, then upwelling mantle may cross the wet-olivine solidus producing hydrous partial melt. The melt density is thought to be denser than the upper mantle, but less dense than the transition zone thus permitting the melt to perch upon the 410-km density increase. The water-filter model suggests this deep melting dynamically creates MORB and OIB chemical signatures, obviating the need for preexisting chemical reservoirs.

[3] There are four key requirements to make this model function: the transition zone must be adequately hydrated (~0.1–2%); the olivine water solubility contrast across the d410 must be >3; the density of the hydrous melt must be in between that of olivine and wadsleyite; and the grain-scale melt topology must be connected to permit porous flow. Recent measurement of the electrical conductivity of the transition zone requires >0.3% water which is marginally sufficient to produce hydrous melting across the d410 [*Huang et al.*, 2005]. A simple global water-filter model calculation that assumes a 1 mm/yr upwelling rate suggests that the melt layer would have 0.1–1.5% melt porosity and a thickness of 2–20 km [*Bercovici and Karato*, 2003]. Thicker and higher porosity melt layers could develop where upwelling rates and/or transition zone hydration levels are enhanced.

[4] This potential melt layer is expected to be manifest as a low-velocity layer atop the 410-km discontinuity (termed the 410-LVL). The velocity reduction within the 410-LVL is expected to be roughly proportional to the melt porosity within the molten layer [*Kreutzmann et al.*, 2004]. First-order seismic constraints with respect to the 410-LVL that would help to test and constrain the water-filter hypothesis would be (1) the velocity decrement of the 410-LVL with respect to the overlying mantle, (2) the width of the 410-LVL, (3) the sharpness of the velocity gradient at the top of the melt layer, and (4) the sharpness of the velocity gradient of the 410-km discontinuity.

[5] Previous regional observations have found a 410-LVL beneath coastal China [*Revenaugh and Sipkin*, 1994], the Pacific northwest region of the United States [*Song et al.*, 2004], the Arabian plate [*Vinnik et al.*, 2003], Siberia [*Vinnik et al.*, 2004] and northern Mexico [*Gao et al.*, 2006]. These studies find a 410-LVL with a 3–7% shear wave reduction and a layer thickness between 90 km and the vertical resolution limit of the data (~20 km). From a global perspective, the 410-LVL is only rarely observed in the analysis of P to S conversions [*Lawrence and Shearer*, 2006] and underside P_dP and S_dP reflections [*Flanagan and Shearer*, 1998]. Nonobservation of the 410-LVL may be related to inadequate data-fold, lower frequencies, or large Fresnel zones of underside reflections. However, because of the conditions necessary for operation of the water-filter model, nonobservations of a 410-LVL most probably reflects that it is not a global phenomenon.

[6] In this study, we achieve a vertical resolution of 6 km using 5 s dominant period converted S-wave arrivals. We find that the 410-LVL under the northern Rockies has an 8.9% shear velocity reduction and is 22 km thick, which is at the extrema of previous estimates. We believe that the difference in our 410-LVL constraints, with respect to previous studies, reflects our use of three densely instrumented broadband seismic arrays. The high-fold stacking among the stations in each array provided excellent quadrant stack error estimates that permit fine-scaled velocity models for the 410-LVL to be accurately constrained.

2. Data and Methods

2.1. Arrays and Earthquakes

[7] To constrain the seismic properties of candidate 410-LVL arrivals, teleseismic data from three IRIS-PASSCAL arrays that operated for 10-month periods in the northern Rocky Mountain are analyzed (Figure 1). The thirty stations that comprise each of the seismic arrays provide an unparalleled opportunity to beam-form relatively short period P-coda to robustly isolate P to S conversion from mantle shear wave discontinuities. Earthquake locations are suitably distributed to permit each array to provide three well-resolved quadrant-stacks from the NW, SE and SW back-azimuth quadrants (Figure 2). The NW and SE quadrants have a sufficient range of earthquake distributions which allows for excellent moveout analysis.

2.1.1. Source Deconvolution

[8] Radial and tangential component receiver functions are calculated using frequency domain water-level deconvolution [*Clayton and Wiggins*, 1976; *Vinnik*, 1977]. The optimal water level is chosen as the "elbow value" in a variance versus misfit plot. The mean water level used in calculating the receiver functions is 0.09 htz-m/s^2, with a standard deviation of 0.04. A second order Butterworth band-pass filter with corners at 3 and 30 seconds is applied to the deconvolved traces. To account for

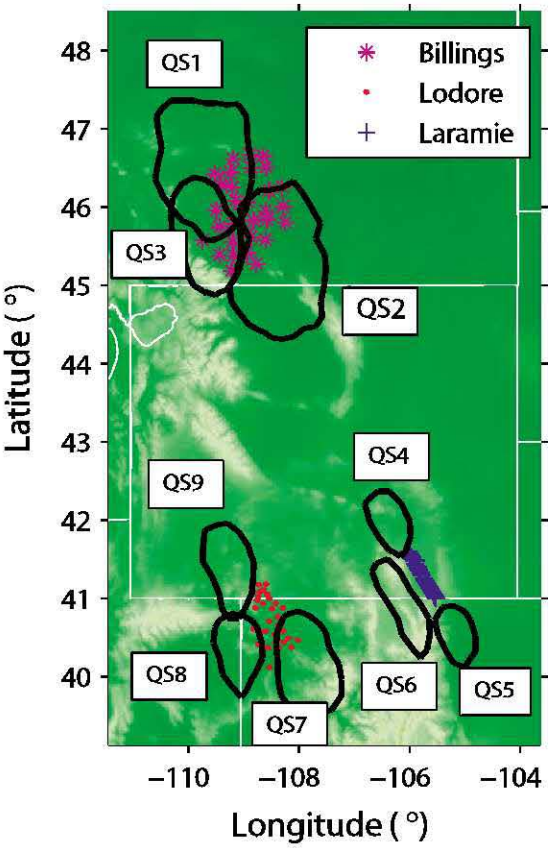

Figure 1. Seismic arrays, sampling of 410-km discontinuity, and topography. Black lines contour the piercing points of the P-S conversions at 410-km depth for the three well-sampled back-azimuth quadrants (NW, SW, and SE) for each of the three seismic arrays denoted in the legend. Labels correspond to the quadrant stack (QS) number referred to in the text and subsequent figures. Each array consisted of 30 broadband seismic stations operating for 10 months.

filtering effects on the data caused by the deconvolution and the post-deconvolution Butterworth filter, the filtered vertical component receiver functions for the entire set of data are stacked to create a mean impulse response estimate (Figure 3). This wavelet is convolved with the synthetic seismograms to properly account for these effects. The side lobes of the estimated wavelet are just under 20%, significantly less than the amplitude ratio of the 410-LVL and the 410-km discontinuity arrival (Figure 4). Sidelobes are accounted for in the modeling procedure through convolution with the synthetic seismograms calculated from velocity models.

2.1.2. Data Culling

[9] The useable receiver functions in each of the nine back-azimuth quadrants are selected by requiring that the standard deviation of each receiver function be within 1.5 standard deviations of the mean standard deviation for each quadrant stack. In addition, visual inspection is used to remove any receiver functions containing glitches and/or oscillatory signal. Each quadrant stack is calculated by taking the mean of 100–200 moveout corrected receiver functions. The data comprising each quadrant stack are distributed normally within two standard deviations of the mean (Figure 5). Beyond two standard deviations fat tails are observed which is expected and will bias our Gaussian distribution based spread estimates toward higher values. To avoid any parametric assumption about the functional form of the error distribution, standard errors are therefore calculated via bootstrapping of the data [*Martinez and Martinez*, 2001].

2.1.3. Velocity Models

[10] Receiver function time is mapped to depth using the western U.S. TNA shear wave model [*Grand and Helmberger*, 1984] modified to have a crustal thickness consistent with local array con-

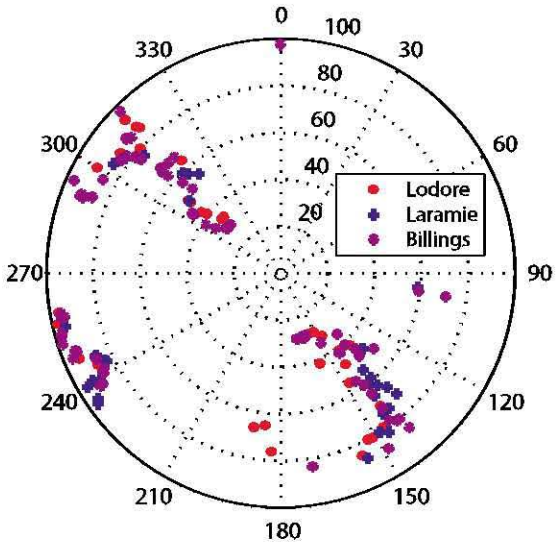

Figure 2. Teleseismic earthquake source distribution for three arrays. Earthquakes used are plotted with respect to back-azimuth and earthquake distance in degrees. The NW and SE quadrants show an excellent distribution of sources with respect to distance which permits reliable moveout analysis. The SW quadrant event distance range distribution is too limited to warrant moveout analysis.

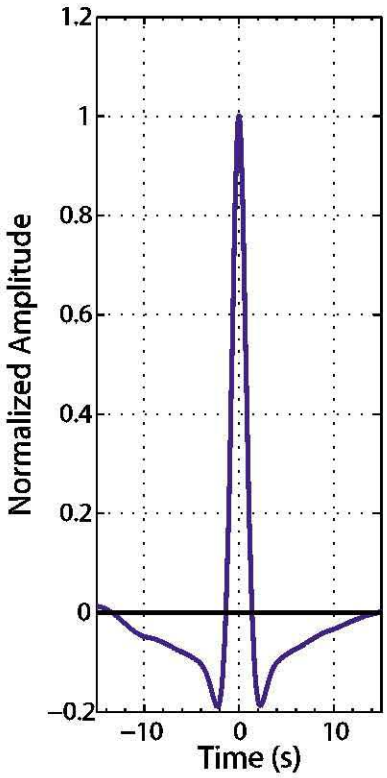

Figure 3. Normalized average vertical receiver function. The average normalized vertical receiver functions for each quadrant stack are averaged together, forming a mean vertical receiver function that is convolved with the synthetic seismograms. The resulting estimated impulse response is symmetric with side lobes just under 20%.

straints [*Crosswhite and Humphreys*, 2003; *Yuan et al.*, 2006]. V_p/V_s was fixed to 1.76 in the crust and the mean IASPI upper mantle value of 1.81 was used for the mantle. Teleseismic tomographic images beneath the three arrays show only modest velocity variations in the upper 150 km [*Yuan and Dueker*, 2003, 2005].

2.2. Mantle Discontinuity Signals

2.2.1. Radial Receiver Functions

[11] The most remarkable feature in the quadrant stacks is a large negative polarity arrival (the 410-LVL arrival) that precedes and interferes with the positive d410 arrival in quadrant stacks 1–7 (Figure 4). These arrivals show no obvious correlation with the amplitude of d410 and d660 arrivals or transition zone thickness (Table 3). We observed that the d410 arrival pulse shape is broadened in quadrant stacks 2,3,6,8 and 9. However, no correlation between pulse broadening and the d410 amplitude or depth is apparent. The d660 pulse shape and arrival depths are relatively uniform in quadrant stacks 1–7. Quadrant stacks 8 and 9 display broadened d660 pulse shapes and decreased amplitudes with the d660 arrival in quadrant stack 9 having a secondary positive arrival at 720 km depth.

2.2.2. Tangential Receiver Functions

[12] The tangential component quadrant stacks generally have low amplitudes suggesting the absence of large anisotropic velocity contrasts or interfaces dipping at >10° (Figure 6). Where significant tangential energy exists, little phase coherence exists between the radial and tangential receiver functions. The largest tangential arrival (2% of direct P amplitude) is observed at 410-LVL depths from the SW back-azimuth quadrant stacks 3 and 6. It is worth noting that the SW back-azimuth quadrant stacks lack a distribution of source distances (Figure 2) and are thus more prone to contamination by local signal generated noise.

2.2.3. Moveout

[13] Moveout analysis of the NW and SE quadrant events shows that the 410-LVL, d410, and d660 arrivals all display the correct moveout for P_ds arrivals (Figure 7). Each quadrant stack moveout analysis is also robust with respect to analysis of random disjoint halves of the data set (Figure 8). Remarkably, the d410 arrival is anomalously deep (437 km) in quadrant stack 4. The depressed d410 arrival displays the correct moveout (Figures 4 and 7). We believe the depth anomaly is not due to velocity effects above 410-km depth for two reasons: (1) the 660-km discontinuity depth is not correspondingly depressed as would be expected for a velocity effect above the 410-km discontinuity; (2) the measured relative teleseismic P wave residuals from the Laramie array show maximum peak to peak variations of 0.9 s which are far too small to create the d410 arrival depression [*Yuan and Dueker*, 2003]. In addition, reasonable transition zone shear velocity perturbations of ±3% [*Ritsema et al.*, 2004], assuming correlated compressional wave velocity changes, only perturbs the d410 depth by 5 km. Bootstrapping the 101 receiver functions comprising quadrant stack 4 into a set of 1000 new quadrant stacks reveals a distribution with mean d410 depth of 441 km and standard deviation of 3 km. In addition, visual inspection of the data does not reveal any spuriously offset data in the quadrant stack. Thus the deep d410 arrival is

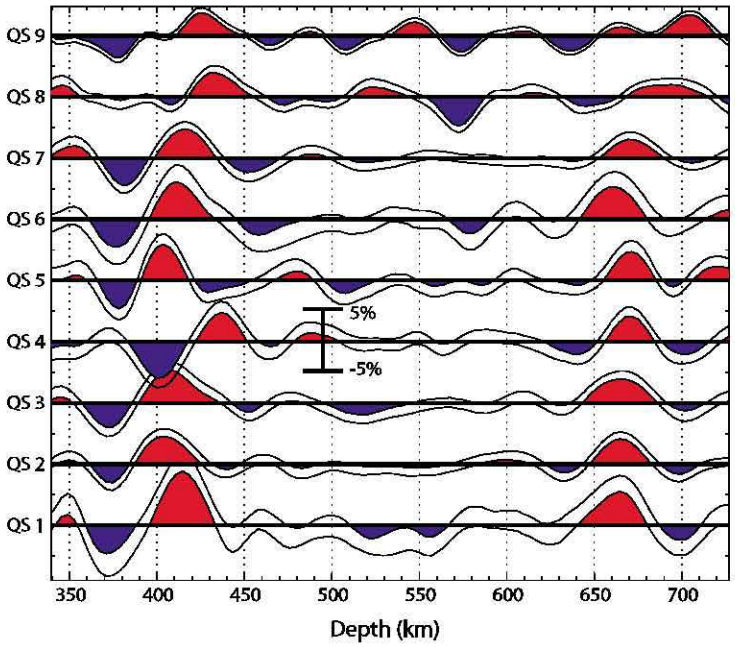

Figure 4. Radial receiver functions for nine quadrant stacks mapped to depth. The receiver function quadrant stack locations are labeled in Figure 1. One standard deviation of the signal is demarcated by the double lines with amplitudes greater than one standard deviation in amplitude shaded. The vertical scale symbol shows a 10% amplitude variation relative to the vertical P wave amplitude. A variation of 32 km in the depth of the d410 arrival is observed both between and within the three arrays (Figure 1). A negative polarity arrival just above the positive d410 arrival is observed on QS 1–7. QS 8 does not have a 410-LVL arrival, and QS 9 shows a negative polarity arrival offset to shallower depth. For QS 1–7 the depth of the d660 arrival is near IASPI91 predictions.

a real attribute of the data and its interpretation is discussed in the Results section.

2.3. Methodology

2.3.1. Double Gradient Slab Velocity Model Parameterization

[14] In this paper, we focus on modeling the seven interfering 410-LVL and d410 arrivals seen in quadrant stacks 1–7 (Figure 4). In contrast, the 410-LVL and d410 arrivals in quadrant stack 9 are separated by 50 km, while for quadrant stack 8 the 410-LVL arrival is not observed.

[15] To model the 410-LVL waveforms, a simple five-parameter velocity model which we call the double gradient slab model is used (Figure 9). The five model parameters are defined as (1) top gradient (TG), which is the thickness of the top negative velocity gradient, (2) shear velocity decrease (dV_s-TG) of the top velocity gradient, (3) bottom gradient (BG), which is the thickness of the bottom positive velocity gradient, (4) shear velocity increase (dV_s-BG) of the bottom gradient, and (5) the thickness of a constant velocity slab (ST) sandwiched between the two velocity gradients. Note that the dV_s-BG parameter is defined as the velocity increase of the bottom gradient with respect to the IASPI91 reference model (Figure 9).

[16] The slab dimension parameters TG, BG and ST ranged from 0 to 45, 35, and 55 km, respectively, in 5 km increments. The velocity gradient dV_s-TG ranged from −0.80–0.0 km/s in 0.08 km/s increments and the velocity gradient dV_s-BG ranged 0.0–1.7 km/s in 0.17 km/s increments.

[17] A grid search is evaluated over the 116,160 velocity models in this five-parameter space. Synthetic receiver functions are calculated for the double gradient slab velocity models with a reflectivity code [*Park*, 1996] using the mean ray parameter value of 0.06 s/km from the data set. To account for the filtering effects applied to our data, the synthetics are convolved with our estimated effective source wavelet (see above). Our modeling does not attempt to match the absolute time of the arrivals and only fits the waveform of the 410-LVL and d410 arrivals. The optimal time lag between the observed and synthetic waveforms is found using cross-correlation and is used to shift the synthetic waveform into alignment with the data before misfit norms are calculated.

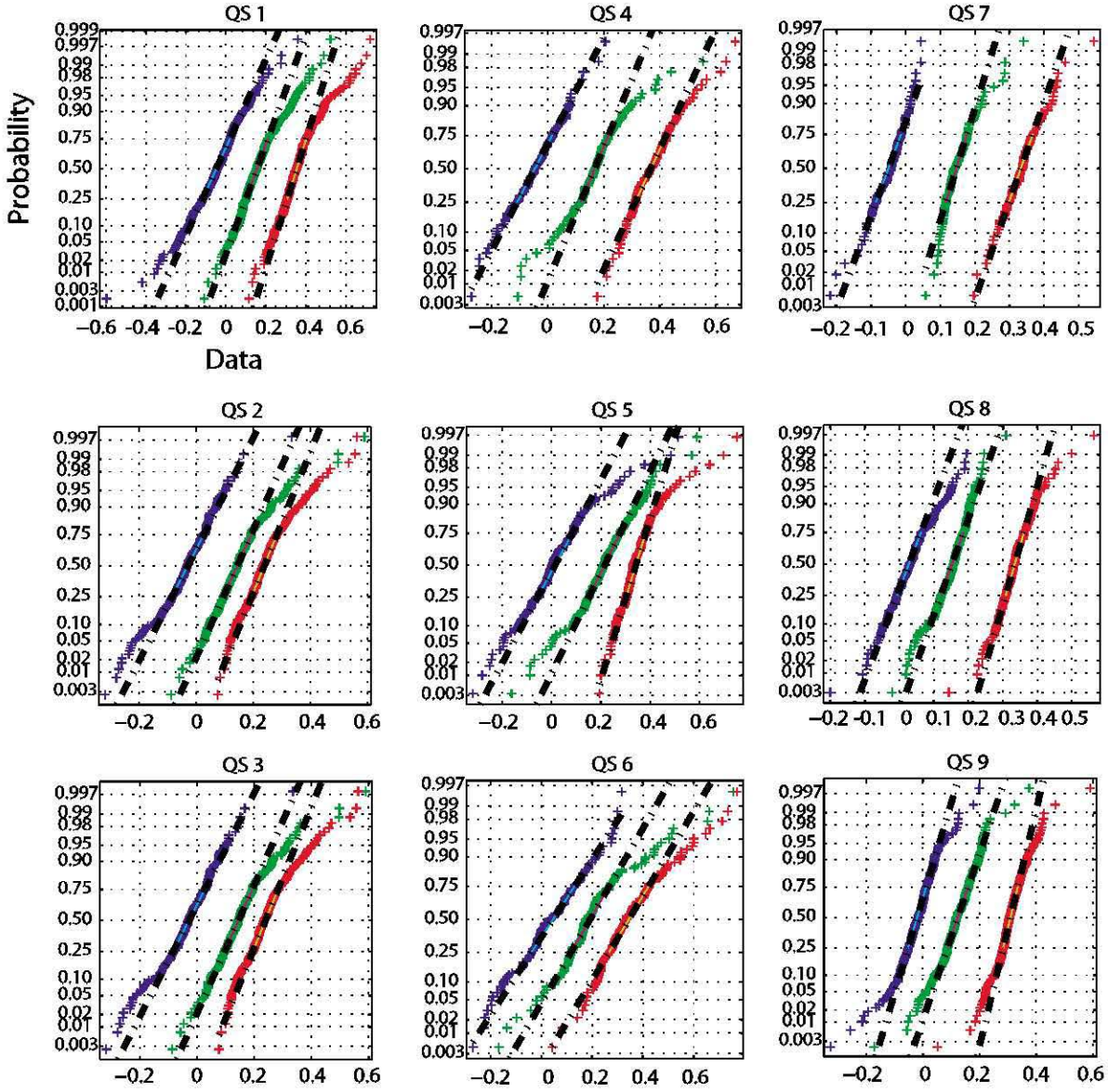

Figure 5. Test of data normality. A Gaussian probability distribution was fit to samples at the peaks of the 410-LVL, d410, and d660 arrivals. For clarity, data marked by green and red have been shifted by 0.1 and 0.3 s (in QS 4, 5, and 8 the shift is 0.2 and 0.3 s). The blue, green, and red plus symbols represent the sample value at the peaks of the three arrivals. If the data are normally distributed, the data will plot along the black dashed line. The slope of this line is proportional to the standard deviation, and the data value at which the line crosses a 0.5 probability is the mean of the data. In each case the data follow a normal distribution out to two standard deviations, after which fat tails are observed.

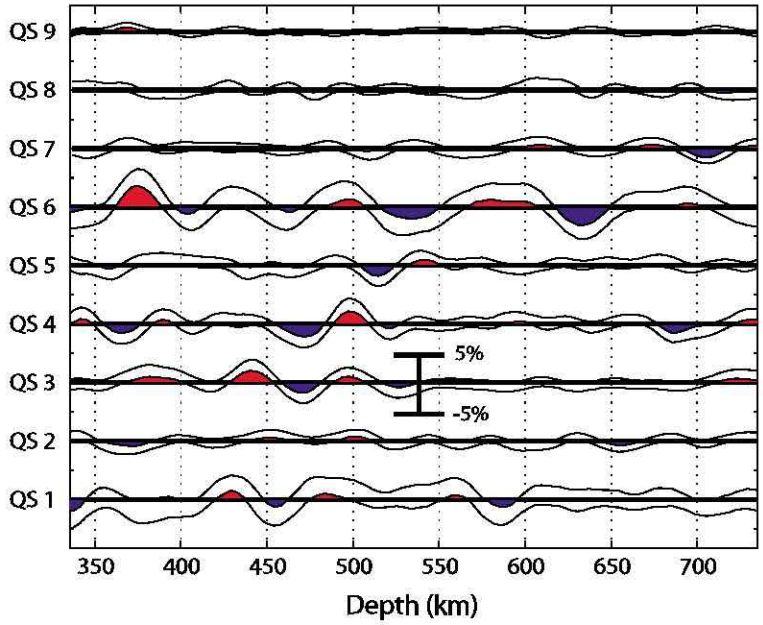

Figure 6. Tangential receiver functions. The one standard deviation error widths are represented as the double lines for each QS. The vertical scale symbol denotes 10% amplitude range relative to vertical P wave. The small amplitudes in the tangential QS are consistent with a lack of significant anisotropic velocity variations or dipping layers.

2.3.2. Calculation of Posterior Marginal Probability Distribution Functions

[18] To assess whether or not the data has a Gaussian distribution, Gaussian probability plots have been constructed for the peaks of the 410-LVL, d410 and d660 arrivals (Figure 5). Inspection of these plots shows that within two sigma of the mean (between 5% and 95% probability on the y axis), the data are normally distributed. Beyond two standard deviations from the mean, "fat" probability tails are observed which will bias our error bars to be larger than "normal." Therefore we believe that the use of a L^2 norm to quantify misfit is justified.

[19] The fit of each model to the data is quantified using a Gaussian likelihood function

$$L(\mathbf{m}) = k \exp\left(-\frac{1}{2}(\mathbf{d}-\mathbf{g}(\mathbf{m}))^T C_D^{-1}(\mathbf{d}-\mathbf{g}(\mathbf{m}))\right),$$

where $\mathbf{d}$ is the observed quadrant stack data, $\mathbf{m}$ is the double gradient slab model, $\mathbf{g}(\mathbf{m})$ is the synthetic receiver function for model $\mathbf{m}$, and C_D^{-1} is the inverse data covariance matrix [*Sambridge*, 1999]. The probability of a model, given a data vector $\mathbf{d}$, is defined as $P(\mathbf{m}|\mathbf{d}) = k\rho(\mathbf{m})L(\mathbf{m}|\mathbf{d})$ where k is an irrelevant scaling factor and $\rho(\mathbf{m})$ is an a priori model distribution. The a priori model distribution parameter is set to unity since all models are considered equally likely.

[20] The likelihood function $L(\mathbf{m})$ thus defines a 5-D error volume containing all the information on model uncertainties and model parameter trade-off. To visualize the 5-D probability volume, 1- and 2-D marginal probability distributions for individual model parameters are calculated. The 1-d marginal probability distribution function is defined as

$$M_1(m_i) = \int \cdots \int P(\mathbf{m}) \prod_{\substack{k=1 \\ k \neq i}}^{d} dm_k$$

where d is the number of model parameters. The two-dimensional marginal probability distribution is defined similarly as

$$M_2(m_i, m_j) = \int \cdots \int P(\mathbf{m}) \prod_{\substack{k=1 \\ k \neq i,j}}^{d} dm_k.$$

[21] The 2-D marginals allow a visual assessment of correlations between any two model parameters, whereas the 1-D marginals provide the probability density for each model parameter.

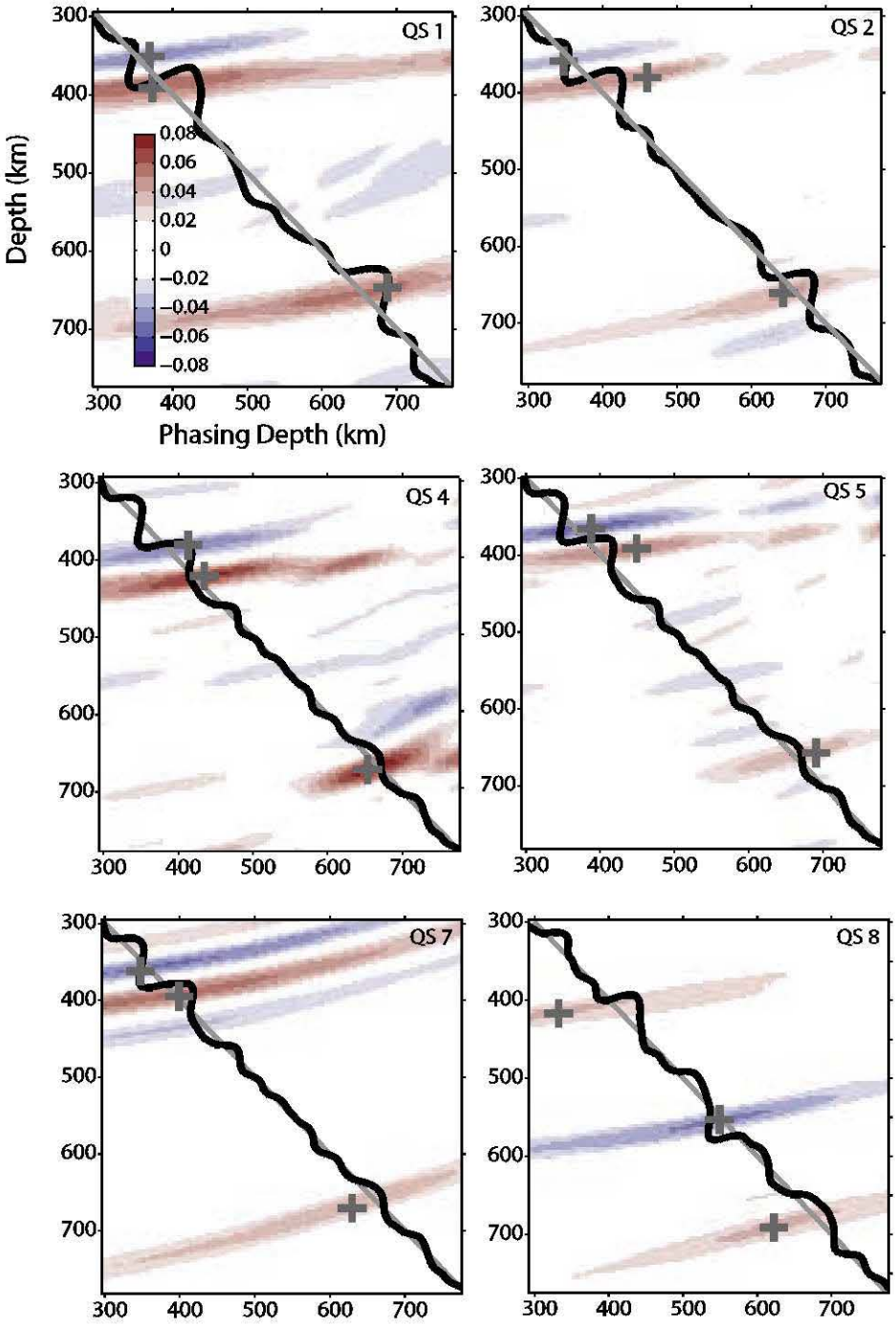

Figure 7. Moveout analysis of the NW and SE quadrant stacks. The amplitude scale with respect to vertical P wave amplitude is the same for each plot. The gray lines have a slope of one along which the amplitude of P to S conversions should be maximal. Solid black lines are thus the optimal phased QS shown in Figure 4. The results demonstrate that the 410-LVL, d410, and d660 signals display moveout consistent with direct P-to-S conversions. The grey plus symbols correspond to the maximal QS amplitude for the arrivals. For QS 8 a negative polarity P to S arrival at 570-km depth displays the correct moveout.

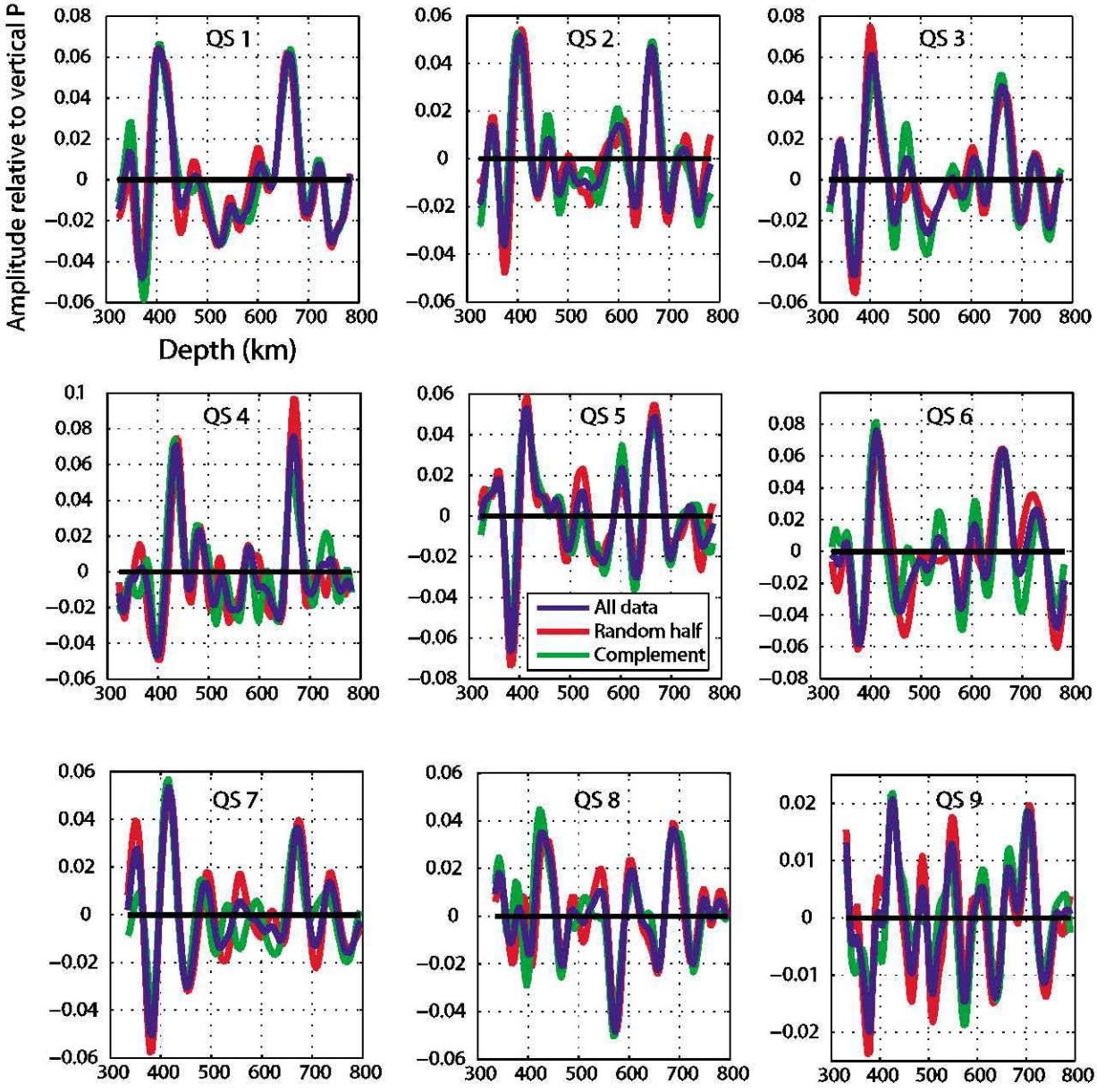

Figure 8. QS waveform stacks with respect to data subsetting. The blue trace is the QS. The 100–200 seismograms in each QS are randomly divided into two disjoint halves and stacked (plotted in red and green). This demonstrates that the 410-LVL, 410, and 660 signals are robustly isolated via stacking.

2.3.3. Synthetic Examples

[22] To assess the resolving power of the grid search, synthetic waveform data sets were calculated with two different double gradient slab models and modeled (Table 1). Random Gaussian noise with a standard error equal to the mean standard error of each quadrant stack is added to each synthetic. For both synthetic data sets, the input double gradient slab model parameters are well recovered by the grid search as evidenced by peaked, unimodal and compactly supported 1- and 2-D marginal probability density functions (Figure 10).

2.3.4. Attenuation Effects

[23] Our synthetic seismograms are purely elastic and do not account for attenuation of the waveforms. For a dominate shear wave period of 5 s and

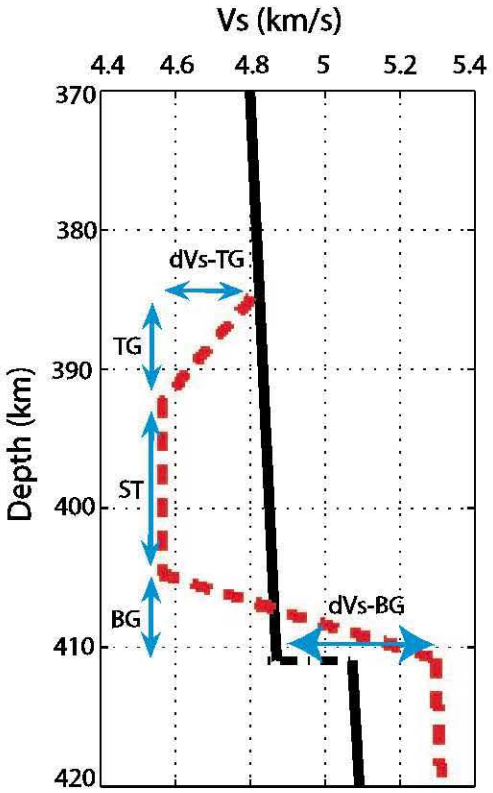

Figure 9. Double gradient slab (DGS) model parameterization. The IASPI91 velocity model is indicated by the solid black line with an example DGS velocity model indicated by the dashed red line. The five model parameters are TG, top gradient thickness (km); ST, constant velocity slab thickness (km); BG, bottom gradient thickness (km); dV_s-TG, shear wave velocity decrease for top gradient (km/s); and dV_s-BG, shear wave velocity increase for bottom gradient (km/s). The value of dV_s-BG is the velocity increase with respect to the IASPI91 model value immediately above the 410-km velocity step.

a nominal slowness of 0.06 s/km, Q_s values for the 410- and 660-km upper mantle converted s-wave paths associated with the $P_{410}s$ and $P_{660}s$ phases predict a t* of about 2 s [*Liu*, 2003]. Amplitude attenuation of the converted S-waves is thus expected to be less than 5% of the elastic converted wave amplitudes [*Aki and Richards*, 2002].

3. Results

3.1. The 410 Low-Velocity Layer

[24] The best fitting synthetic waveform for each quadrant stack lies within one standard deviation of the observed quadrant and fits the peaks and troughs of the observed waveforms very well (Figure 11). Reduced chi-square values around unity demonstrate that the waveforms are generally well fit by the double gradient slab models (Table 2). For the broadest d410 pulse shapes, the double gradient slab model does not fit the entire waveform as well. This observation is reflected by the larger reduced chi-square values (Figure 11 and Table 2). To calculate the reduced chi-square values, the number of degrees of freedom (DOF) in the time series is estimated from the bandwidth of the data [*Silver and Chan*, 1991]. This analysis shows that 1 second of data is about 1 DOF which suggests that the number of DOF for each 15 sec segment that captures the 410-LVL arrival is 15.

[25] Inspection of the 1-D marginal probability density functions shows that the distributions are generally unimodal, indicating that the model parameters are well resolved (Figure 12). The 2-D marginal probability density functions show that some trade-offs exist between model parameters. For example, an anti-correlation of the top and bottom gradient thickness and slab thicknesses is a common observation (Figure 12).

[26] Overlaying the seven 1-D marginals shows significant variations in the model parameter probability density functions (Figure 13) of the bottom gradient thickness and velocity increase parameters. We suggest that the variations are real and manifest the effect of water upon the olivine to wadsleyite phase transition. Remarkably, the top velocity gradient thickness and velocity step show significant overlap of their 1-D marginals. Multiplying these 1-D marginal probability density functions together forms an average 1-D marginal probability density function for the top gradient thickness and its associated velocity decrease (Figure 14). The resulting average probability density functions show that the top gradient is sharp (<6.4 km) and the shear wave velocity decrement is large (0.44 km/s or an 8.9% reduction). To quantify

Table 1. Synthetic Data Results: "Sawtooth" and "DGS" Velocity Models

	TG, km	BG, km	ST, km	dV_s-TG, km/s	dV_s-BG, km/s
			Sawtooth		
Input	5	25	5	−0.3371	0.5056
Recovered	5	25.0	4.9495	−0.3405	0.5107
			DGS		
Input	0	5	25	−0.3371	0.5056
Recovered	0	5	25.10	−0.3405	0.5107

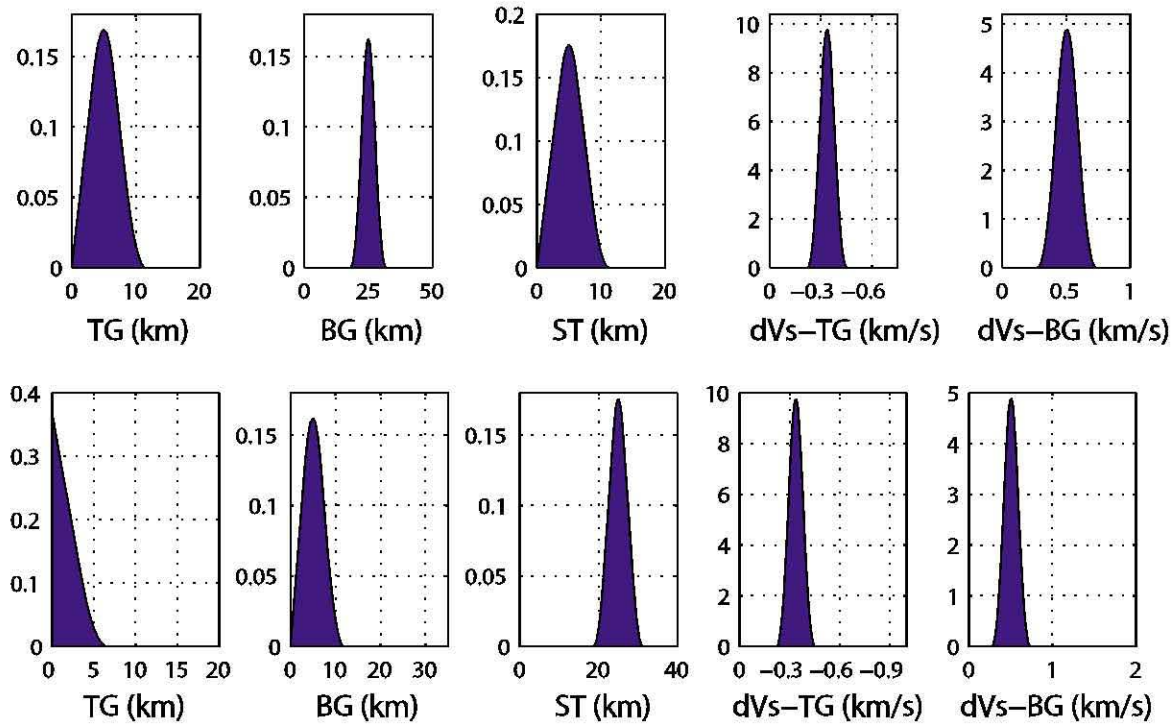

Figure 10. Synthetic data tests. To demonstrate the resolution of our data set, two different synthetic data sets were generated and fitted by our grid search (Table 1). Random noise was added to the synthetic trace data scaled to the observed QS noise levels. In both synthetic tests the 1-D distributions are unimodal with compact support with peaks at the input parameter values (Table 1).

model parameter uncertainty, the 90% probability intervals about the peak of these average 1-D marginal probability density functions are calculated (Figure 14).

[27] Inspection of the other model parameters reveals qualitative similarities among the seven modeled quadrant stacks. In five cases, the bottom gradient thickness is 25–45 km. Also, the constant velocity slab thickness is <10 km in five cases. The average bottom gradient shear velocity increase is 0.60 km/s, an 11.8% shear velocity increase (Figure 13 and Table 2). Velocity models producing the best fitting waveforms are of two types: a "sawtooth" with sharp top gradient and diffuse bottom gradient and a "double gradient slab" with a nonzero slab thickness bounded by sharp gradients (Figure 15). Our synthetic tests verify these two types of velocity models are resolvable by the grid search. To define an effective thickness for the 410-LVL, the mean constant velocity slab thickness (6 km) is added to half the mean thickness of the top and bottom velocity gradients (2 km and 14 km, respectively). This defines a mean 410-LVL thickness of 22 km (Table 2).

3.2. Transition Zone

3.2.1. The 410-km Discontinuity

[28] The bottom shear velocity gradient (dV_s-BG) in the nine quadrant stacks show large variations (Figure 13 and Table 2). In quadrant stacks 2, 3, 5, 7 and 8 the shear velocity increase at d410 varies between 7% and 14%. This velocity change is proportional to the olivine content [*Li et al.*, 2001]. An olivine content of 57–87% is consistent with six of our nine shear velocity steps.

[29] For quadrant stacks 1 and 6, the modeled shear velocity increases of 1.35 km/s and 0.83 km/s are too large for even a 100% olivine mineral assemblage. These large seismic amplitudes can be explained as focusing of the wavefield by 100–200 km wavelength discontinuity topography with 20 km amplitudes [*van der Lee et al.*, 1994]. Our quadrant stack results show that 10, 14, and 33 km of 410-km discontinuity topography is present within each of our three arrays (Figure 4 and Table 3). In addition, 30 km of 410-km discontinuity topography has been found beneath nearby arrays supporting the conclusion that topographic

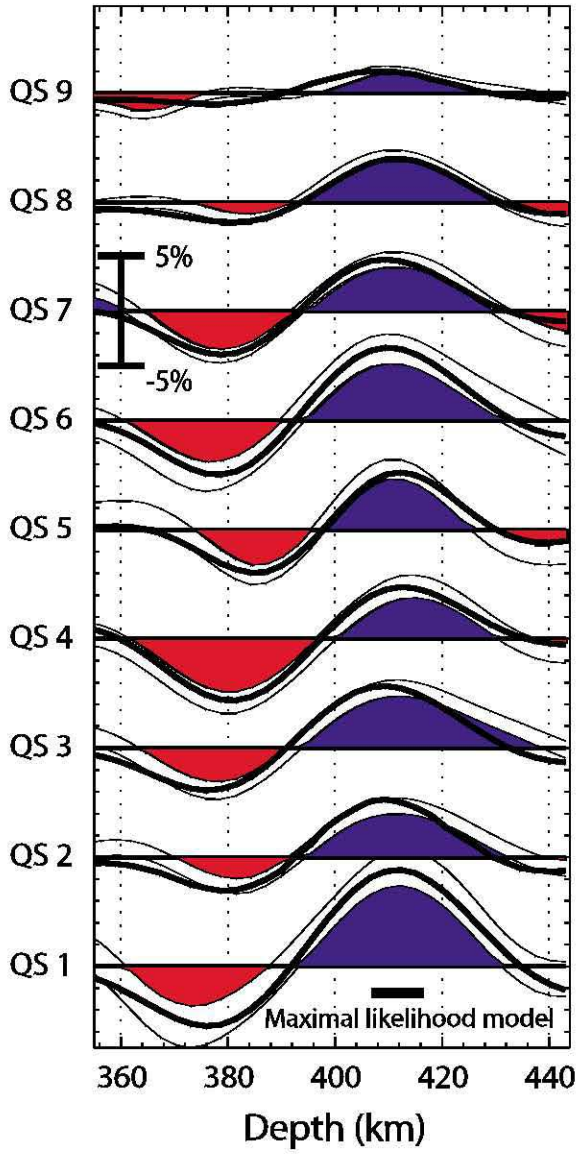

Figure 11. Overlay of best fitting waveforms and observed waveforms. The modeled QS are lined up on the mean 410-km discontinuity depth (416 km). The maximum likelihood model fits the peaks and troughs very well. However, broader d410 arrival pulses associated with QS 2, 3, and 7 are less well fit by the DGS models, as reflected in the chi-square model misfit values (Table 2).

scattering effects are expected [*Fee and Dueker*, 2004; *Gilbert et al.*, 2003].

[30] Conversely, the 1-D marginal for the bottom shear velocity gradient for quadrant stack 4 has a peak value at 0 km/s, or <0.2 km/s at 90% probability (Figure 13 and Table 2). We cannot appeal to wavefield defocusing due to discontinuity topography because the observed 410-LVL arrival amplitude is consistent with the other 410-LVL amplitudes. Therefore we suggest that the velocity gradient is >25 km, which would extinguish the amplitude of converted S-waves [*Bostock*, 1999]. The presence of water is thought to broaden the olivine-wadsleyite transition [*Smyth and Frost*, 2002; *Van der Meijde et al.*, 2003; *Wood*, 1995]. Good evidence for a 410-km discontinuity whose velocity gradients is >25 km is found beneath Russia from the PNE data set [*Priestly et al.*, 1994].

[31] For quadrant stack 4, the d410 arrival is 26-km deeper than the global average. Hydration cannot be the dominant factor in modulating the d410 depth in quadrant stack 4 because water should shallow the d410 arrival, not deepen it [*Litasov et al.*, 2006]. If interpreted as thermal topography, approximately 300°C would be required [*Litasov et al.*, 2006]. With respect to the two nearest quadrant stacks (5 and 6) significant temperature heterogeneity over a 150-km lateral scale is suggested. The normal d660 depth in quadrant stack 4 implies a temperature anomaly that is confined to the upper most transition zone. However, why a thermal anomaly of this magnitude would be isolated here is difficult to explain. Alternatively, we appeal to recent tomographic results of S-velocity structure beneath North America clearly showing the presence of subducted slab at 450-km depth beneath Wyoming [*Bedle and van der Lee*, 2007]. If a piece of sinking slab raises the convective velocity in its wake to greater than the olivine-wadsleyite phase transformation velocity the phase transformation will not occur until a nucleation barrier is overcome. In this case the phase transformation will occur at

Table 2. Results of the Maximum Likelihood Model Calculation for QS 1–9 and Corresponding Reduced Chi-Square Values

	TG, km	BG, km	ST, km	dV_s-TG, km/s	dV_s-BG, km/s	Chi-Square (Reduced)
QS 1	0.0	39.4	14.5	−0.25	1.35	0.91
QS 2	0.0	24.0	0.0	−0.22	0.51	4.3
QS 3	5.5	45.0	0.0	−0.42	0.68	3.7
QS 4	10.0	10.0	25.0	−0.51	0.0	0.22
QS 5	5.0	5.0	5.0	−0.67	0.34	0.82
QS 6	0.0	41.7	0	−0.49	0.83	0.45
QS 7	0.0	44.4	0.0	−0.50	0.51	4.8
Mean (1–7)	**2.9**	**29.2**	**6.4**	**−0.44**	**0.60**	**2.2**
QS 8	0	6.7	0	−0.09	0.51	0.13
QS 9	0	30	0	0	0.35	2.3

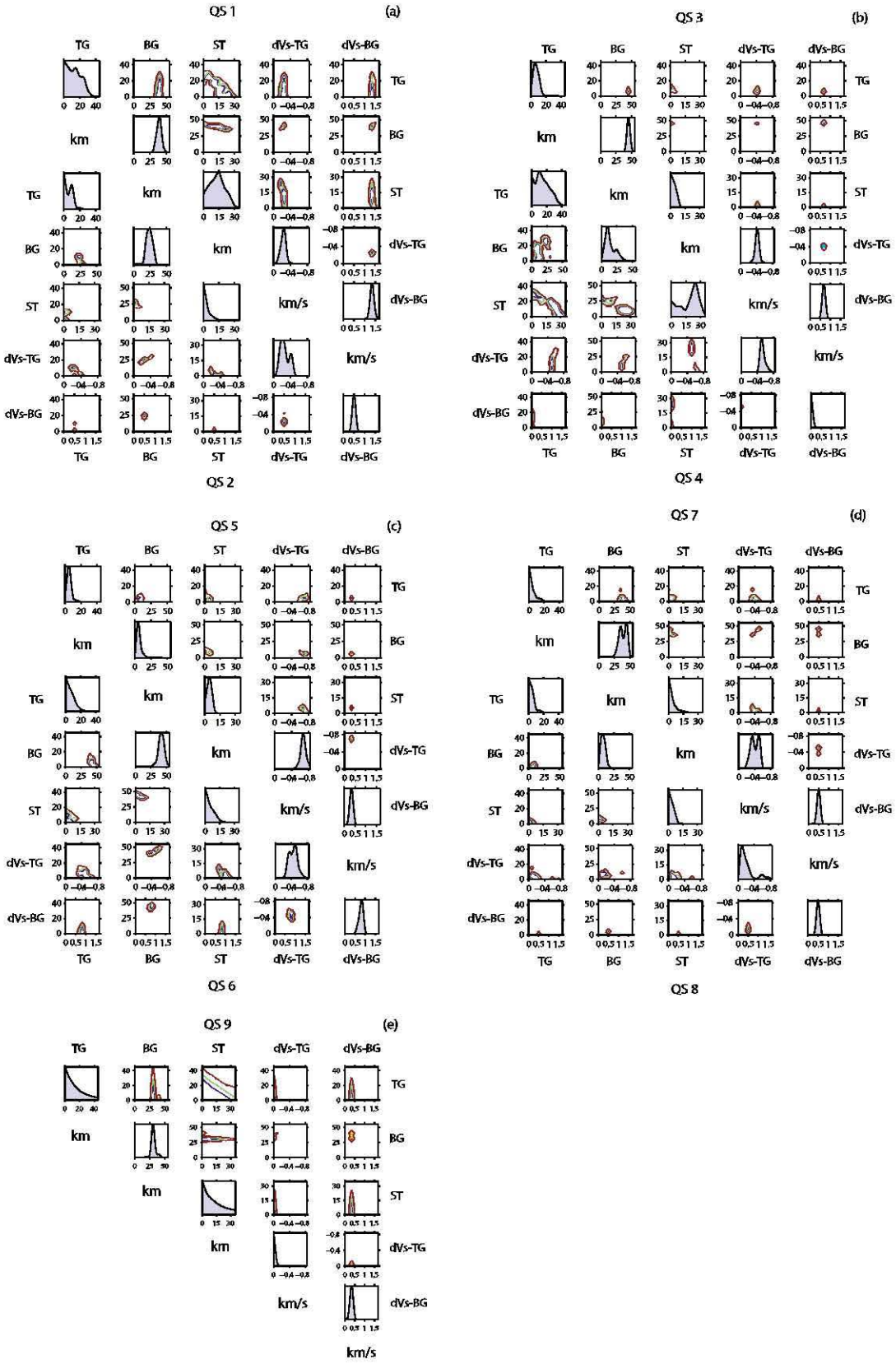
QS 1
(a)
QS 3
(b)
QS 2
QS 4
QS 5
(c)
QS 7
(d)
QS 6
QS 8
QS 9
(e)
TG
BG
ST
dVs-TG
dVs-BG
km
km/s

Figure 12

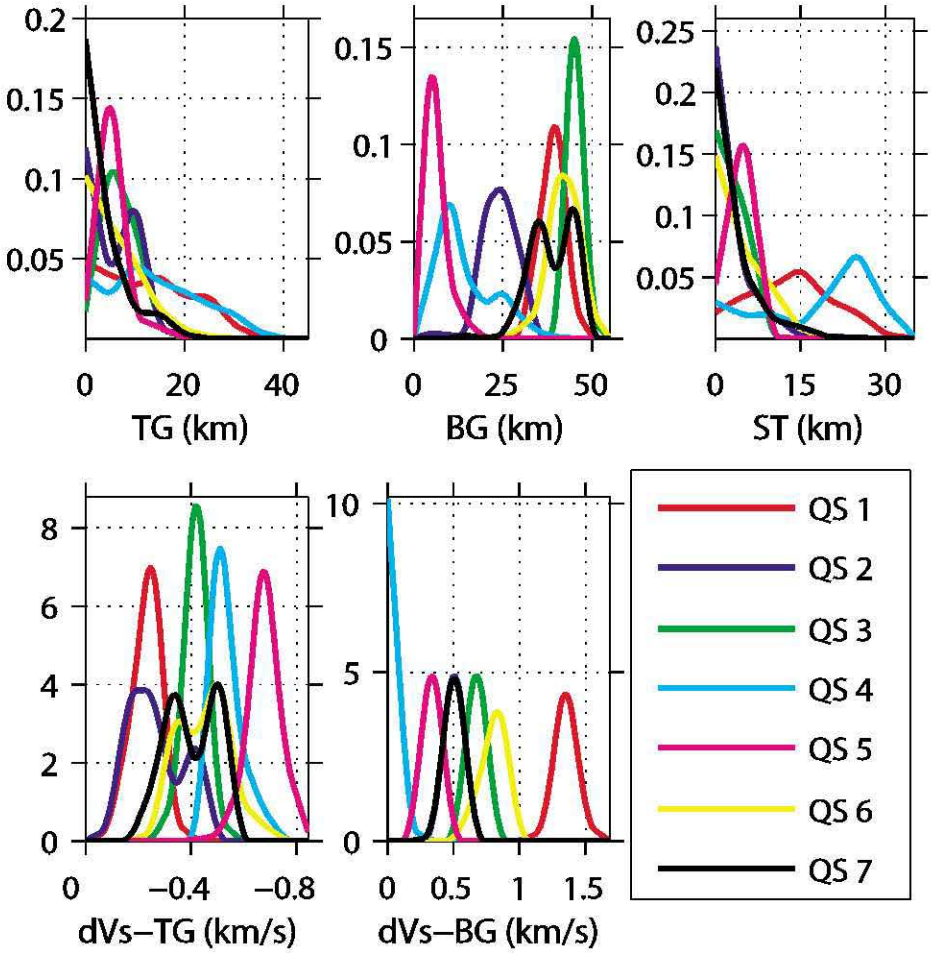

Figure 13. One-dimensional marginal probability distributions for QS 1–7. For each model parameter subplot, the seven 1-D marginal probability distributions are overlain.

an increased depth [*Solomatov and Stevenson*, 1994]. Whether such a process would interfere with the water-filter model and generation of a melt layer is unknown; however, the resulting local topography would create a gravitational well into which nearby melt may pool.

[32] As a test of the stability of the grid search, quadrant stack 8 which does not have a 410-LVL arrival was modeled. The most probable model parameters found by our grid search was as follows: a 0-km top gradient and a 0-km slab thickness, a 6.7-km-thick bottom gradient, and a 0.51 km/s shear velocity increase (Figure 4 and Table 2). This 410-km discontinuity gradient thickness is consistent with the mineral physics predictions of an olivine-wadsleyite transition in an anhydrous, pyrolitic mantle with a phase loop of

Figure 12. One- and two-dimensional marginal probability density functions (PDF) for each quadrant stack. Each of Figures 12a–12d displays plots for two individual quadrant stacks, one above and one below the main diagonal containing the units of the axes for the one-dimensional marginal PDF immediately above and below. The five model parameters are labeled along the row and column space (Figure 9). The two-dimensional marginal PDF at the intersection of a row and column are contoured at the 70, 80, and 90% probability levels and display trade-offs between a pair of model parameters. The marginal PDF are generally unimodal with well-resolved peaks. For example, in quadrant stack 3 a velocity model for which a top gradient corresponds to a velocity decrement near 0 km/s is extremely improbable. The 2-D marginal PDF have minimal correlation between model parameters, with the exception of quadrant stacks 1 and 4, which display correlations between the slab and gradient thicknesses. For quadrant stacks 8 and 9, which lack a 410-LVL arrival, the marginals only characterize the 410-km discontinuity properties.

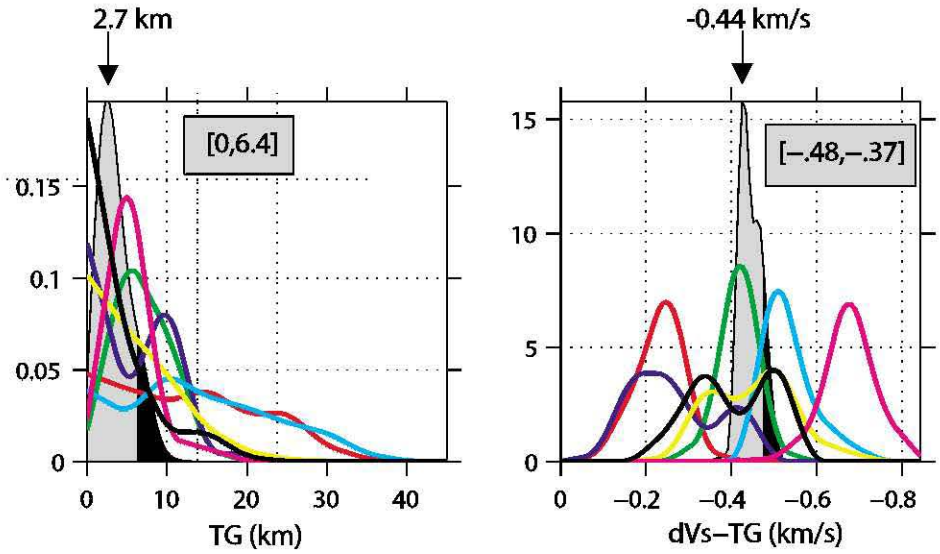

Figure 14. Average 1-D marginals for the top velocity gradient and thickness. The 1-D marginal PDF for the TG and dV_s-TG parameters (Figure 12) significantly overlapped, allowing formation of a summary marginal PDF. The color key is as in Figure 13. The 90% probability interval is shaded gray, and these bounds are labeled. At 90% probability the velocity decrease of the 410-LVL is −0.44 km/s (8.9%) and the top gradient thickness is <6.4 km.

0.3–0.5 GPa [*Litasov et al.*, 2006]. In addition, a very shallow 410-LVL arrival is observed in quadrant stack 9 that is separated from the 410-km discontinuity arrival (Figure 4). The grid search constrains this d410 arrival to have a shear velocity increase of 0.35 km/s: consistent with a pyrolite composition.

3.2.2. The 660-km Discontinuity

[33] The d660 arrivals are well resolved in each quadrant stack with amplitudes requiring a shear velocity contrast up to 0.2 km/s larger than in IASPI91 predictions (9.8% contrast) (Figure 16). On average, the d660 depths are 13 km deeper than the 661-km global average. Noteworthy is that quadrant stacks 8 and 9 are very deep at 694 km and 703 km, respectively (Figure 4 and Table 3) [*Flanagan and Shearer*, 1998; *Gu and Dziewonski*, 2002].

[34] In areas of subduction, d660 depth has been linked to water content via P wave tomography analysis [*Suetsugu et al.*, 2006]. Broadened, multimodal pulse d660 shapes for quadrant stacks 8, 9 may indicate garnet-ilmenite and ilmenite-perovskite transformations in addition to the dissociation of the γ- spinel phase of olivine [*Simmons and Gurrola*, 2000].

3.2.3. Transition Zone Thickness

[35] The transition zone thicknesses vary from 234 km to 277 km with a mean of 257 km (Table 3). This mean transition zone thickness is greater than the global average of 242 km [*Gu and Dziewonski*, 2002], suggesting cooler than normal temperatures within the transition zone. The above average thickness is similar to previously published estimates of higher than average transition zone thicknesses [*Benoit et al.*, 2003; *Gurrola and Minster*, 1998; *Saita et al.*, 2002]. This suggestion of cooler transition zone temperatures beneath our three arrays is consistent with the high-velocity slab fragments imaged in the transition zone [*Bedle and van der Lee*, 2007]. Depths of d410 are near the global average for quadrant stacks 1, 6, 7 and shallower than the global average for quadrant stacks 2, 3, 5 and significantly deeper in quadrant stacks 4, 8, 9. The range of d660 depths are 661–703 km with a mean of 673 km (Table 3).

3.2.4. A 570-km Discontinuity

[36] Quadrant stacks 6, 8 and 9 contain a negative polarity P to S arrival at 570 km that is robust to stacking random halves of the data (Figures 4 and 8). The arrival displays the correct moveout characteristics; however, the limited distribution of earthquakes in quadrant stacks 6 and 9 precludes moveout analysis (Figures 2 and 7). No known phase transition in a pyrolitic mantle occurs at this depth. A 7.4% shear velocity reduction at 570 km produces the observed radial P-to-S amplitude for quadrant stack 8. *Shen and Blum* [2003] found a more pervasive arrival at 570–600 km depth that

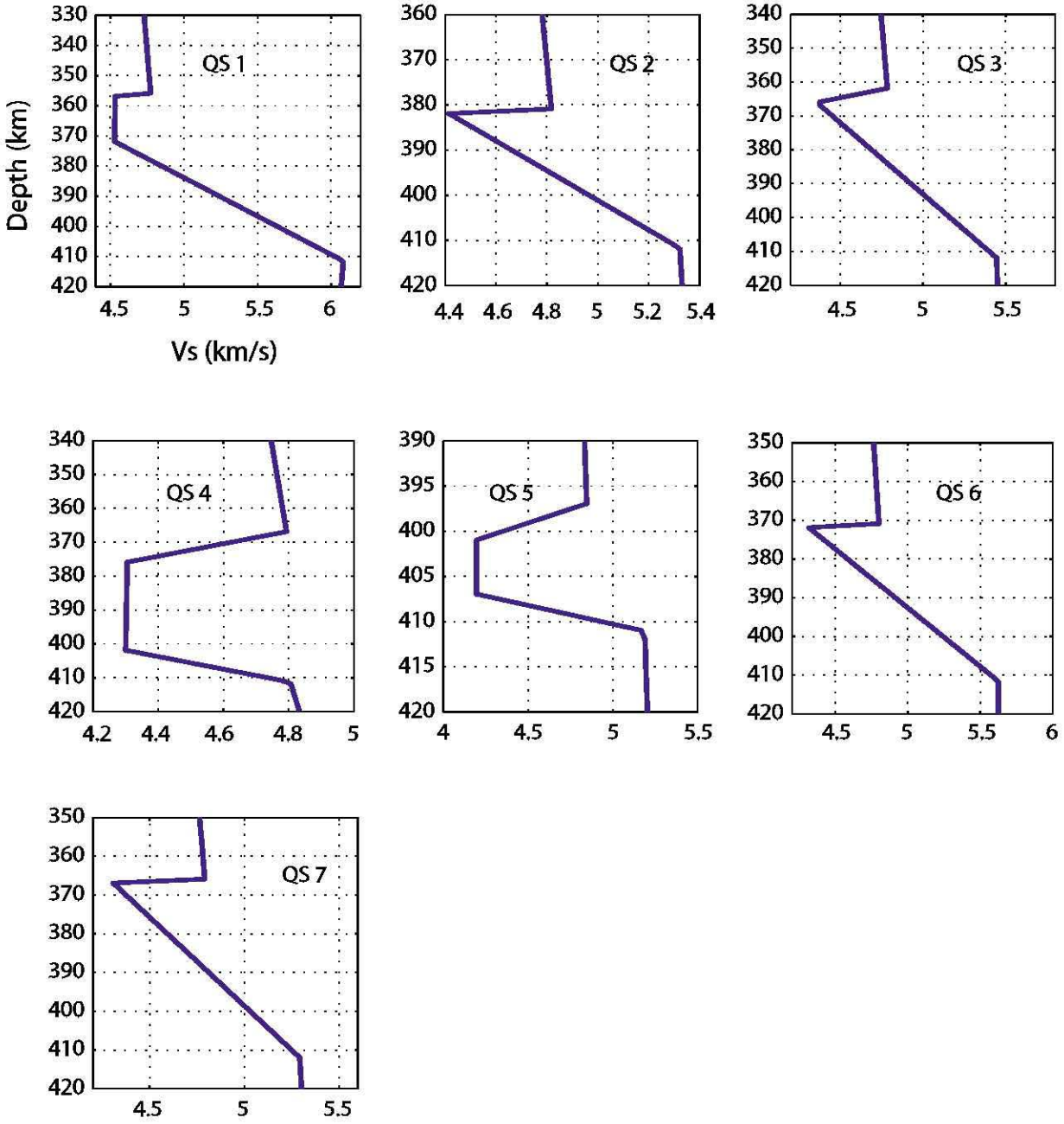

Figure 15. Maximum likelihood velocity models. The maximum likelihood velocity models defined by the 1-D marginal PDF show two basic shapes. For each model a sharp top gradient is observed, and a diffuse bottom gradient is observed in 5 of the 7 models. The grid search of synthetic data shows that these two types of velocity models are resolvable (Figure 10 and Table 1).

was modeled as a 2.2% shear velocity reduction and interpreted as accumulated oceanic crust above d660 [*Shen and Blum*, 2003].

4. Discussion

[37] It is difficult to explain our results as manifesting a process other than a melt layer. It is unlikely that a low-velocity chemical anomaly, such as oceanic crust, is simultaneously stagnated as a horizontal chemical anomaly on the order of 200 km wide in our three widely separated seismic arrays. Noteworthy is that the NA-2007 shear velocity model shows Farallon slab fragments in the transition zone, but these high-velocity anomalies do not cross the 410-km discontinuity [*Bedle*

Table 3. Transition Zone Discontinuity Depths and Transition Zone Thickness

QS	D410 Depth, km	D660 Depth, km	TZ Thickness, km
1	415	665	250
2	404	665	261
3	405	665	260
4	437	671	234
5	404	671	267
6	411	661	250
7	416	669	253
8	430	694	264
9	426	703	277
Mean	**416.3**	**673.8**	**257.4**

and van der Lee, 2007]. Similarly, it is unlikely that the observed 410-LVL is caused by strong anisotropy just above the 410 as systematic variations in the tangential receiver functions are predicted which are not observed. Likewise, a dipping planar layer cannot create a negative polarity radial component arrival and dipping layers would additionally create systematic tangential component variations which are not observed (Figure 6). We therefore suggest that the pervasive 410-LVL observation beneath the northern Rocky Mountains is a manifestation of the water-filter model.

[38] Significant uncertainties remain with regard to the water-filter model. On the basis of simple thermodynamic-gravitational steady state calculations that assumes a 1 mm/yr mantle up-flow rate, the maximal thickness of an equilibrium melt layer is <7 km [*Hirschmann et al.*, 2006]. However, new fundamental and higher mode shear wave velocity images of the transition zone beneath the western U.S. are sufficiently resolved to state unequivocally that remnants of Farallon slab exist beneath our three arrays [*Bedle and van der Lee*, 2007]. Furthermore, the Farallon transition zone slab fragments beneath the western U.S. are apparently folded up and being supported dynamically by the 660-km phase and viscosity transition [*Schmid et al.*, 2002]. A stagnated slab in the transition zone is capable of diffusing out a majority of its water content providing a mechanism to hydrate the transition zone [*Richard et al.*, 2006]. Thus it seems plausible that a wet, and therefore positively buoyant, transition zone upwelled in late Cenozoic time above these slab fragments to produce a thick melt layer atop the 410-km discontinuity.

[39] Our estimated 410-LVL thickness of 22 km is much thicker than quasi-equilibrium global estimates using a 1 mm/yr upwelling rate [*Hirschmann et al.*, 2006]. Three factors can make a thicker melt layer with respect to this model: greater upwelling rates; a more hydrated transition zone; and concave-downward d410 topography that permits the gravitational ponding of melt. We conclude that some poorly constrained combination of these three factors is ongoing in the transition zone beneath the northern Rocky Mountains. Further detailed mapping of the 410-LVL in the western U.S. should permit these three factors to be disentangled in future research.

[40] The relationship between melt porosity and shear velocity reduction is not well constrained at the bottom of the upper mantle. At uppermost mantle pressures, theoretical and laboratory mea-

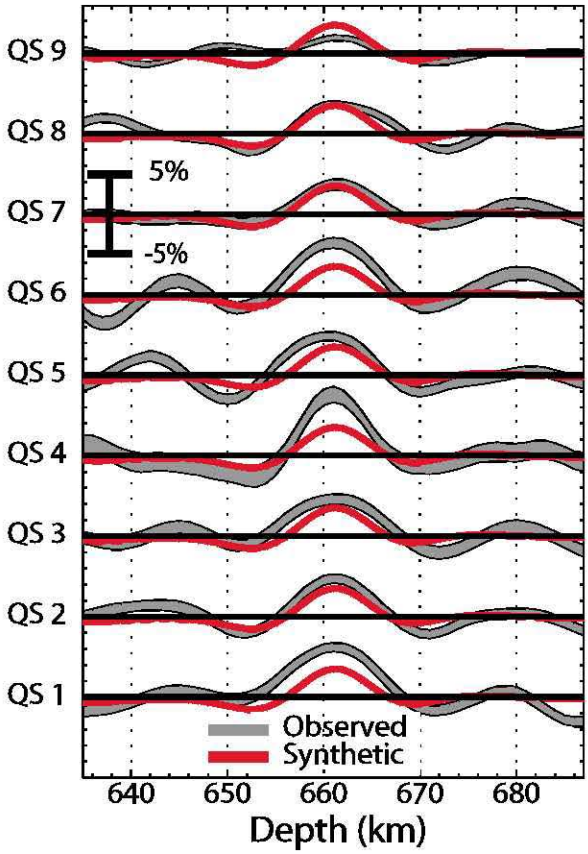

Figure 16. Observed and synthetic 660-km discontinuity arrivals. The vertical scale shows an amplitude range of 10% relative to vertical P wave arrival. The gray swath is the one-sigma bounds of the observed signal, and the red lines are the IASPI91 velocity model predictions for a mean ray parameter of our data set (0.06 s/km). The pulse widths of the observed and synthetic data are similar, although the observed amplitudes are generally higher than IASPI91 predictions.

surements find that 1% melt porosity produce about a 2.2% reduction in shear velocity [*Kreutzmann et al.*, 2004]. However, the effect of water in the melt is expected to lower the viscosity enough to affect the melt-velocity scaling. Given the uncertainties in assessing melt-velocity scalings in the 410-LVL, we simply note that our 8.9% velocity reduction would requires about 4% melt porosity using the uppermost mantle scaling values.

5. Conclusions

[41] In conclusion, this study has constrained the seismic properties associated with the 410-LVL from the modeling of nine well-resolved radial receiver function stacks from three different dense arrays in the northern Rocky Mountains. The top of the 410-LVL is characterized by an 8.9% shear velocity drop over a <6-km linear gradient. The thickness of the layer varies from 10–35 km with a mean value of 22 km (Table 2). Because velocity, temperature and water effects on the 410-LVL have overlapping effects on the transition zone discontinuity properties, accurate transition zone V_p and V_s images will be needed to discriminate the effects of temperature and water as the causes of the short scale length heterogeneity we have found.

Acknowledgments

[42] We would like to thank Andrew A. Nyblade and Anne F. Sheehan for their constructive reviews and comments on this manuscript. We also acknowledge the facilities of the IRIS Data Management System, and specifically the IRIS Data Management Center, for access to the waveform and metadata required in this study.

References

Aki, K., and P. G. Richards (2002), *Quantitative Seismology*, 2nd ed., Univ. Sci., Sausalito, Calif.

Bedle, H., and S. van der Lee (2007), Progress on a new regional model of the upper-mantle S-velocity structure beneath the North American continent, poster presented at EarthScope National Meeting, Natl. Sci. Found., Monterey, Calif.

Benoit, M. H., A. A. Nyblade, J. C. VanDecar, and H. Gurrola (2003), Upper mantle P wave velocity structure and transition zone thickness beneath the Arabian Shield, *Geophys. Res. Lett.*, *30*(10), 1531, doi:10.1029/2002GL016436.

Bercovici, D., and S. Karato (2003), Whole-mantle convection and the transition-zone water filter, *Nature*, *425*, 39–44.

Bostock, M. G. (1999), Seismic waves converted from velocity gradient anomalies in the Earth's upper mantle, *Geophys. J. Int.*, *138*, 747–756.

Clayton, R. W., and R. A. Wiggins (1976), Source shape estimation and deconvolution of teleseismic body waves, *Geophys. J. R. Astron. Soc.*, *47*, 151–177.

Crosswhite, J. A., and E. D. Humphreys (2003), Imaging the mountainless root of the 1.8 Ga Cheyenne belt structure and clues to its tectonic stability, *Geology*, *31*, 669–672.

Fee, D., and K. Dueker (2004), Mantle transition zone topography and structure beneath the Yellowstone hotspot, *Geophys. Res. Lett.*, *31*, L18603, doi:10.1029/2004GL020636.

Flanagan, M. P., and P. M. Shearer (1998), Global mapping of topography on transition zone velocity discontinuities by stacking SS precursors, *J. Geophys. Res.*, *103*, 2673–2692.

Gao, W., E. Matzel, and S. P. Grand (2006), Upper mantle seismic structure beneath eastern Mexico determined from P and S waveform inversion and its implications, *J. Geophys. Res.*, *111*, B08307, doi:10.1029/2006JB004304.

Gilbert, H. J., A. F. Sheehan, K. G. Dueker, and P. Molnar (2003), Receiver functions in the western United States, with implications for upper mantle structure and dynamics, *J. Geophys. Res.*, *108*(B5), 2229, doi:10.1029/2001JB001194.

Grand, S. P., and D. V. Helmberger (1984), Upper mantle shear structure of North America, *Geophys. J. R. Astron. Soc.*, *76*, 399–438.

Gu, Y. J., and A. M. Dziewonski (2002), Global variability of transition zone thickness, *J. Geophys. Res.*, *107*(B7), 2135, doi:10.1029/2001JB000489.

Gurrola, H., and J. B. Minster (1998), Thickness estimates of the upper-mantle transition zone from bootstrapped velocity spectrum stacks of receiver functions, *Geophys. J. Int.*, *133*, 31–43.

Hirschmann, M. M., A. C. Withers, and C. Aubaud (2006), Petrologic structure of a hydrous 410 km discontinuity, in *Earth's Deep Water Cycle*, *Geophys. Monogr. Ser.*, vol. 168, edited by S. D. Jacobsen and S. van der Lee, pp. 277–287, AGU, Washington, D. C.

Huang, X. G., Y. S. Xu, and S. Karato (2005), Water content in the transition zone from electrical conductivity of wadsleyite and ringwoodite, *Nature*, *434*, 746–749.

Kreutzmann, A., G. Marquart, I. T. Bjarnason, H. Schmeling, A. Junge, and T. Ruedas (2004), Temperature and melting of a ridge-centred plume with application to Iceland. Part II: Predictions for electromagnetic and seismic observables, *Geophys. J. Int.*, *159*, 1097–1111.

Lawrence, J. F., and P. M. Shearer (2006), A global study of transition zone thickness using receiver functions, *J. Geophys. Res.*, *111*, B06307, doi:10.1029/2005JB003973.

Li, B., R. C. Liebermann, and D. J. Weidner (2001), P-V-Vp-Vs-T measurements on wadsleyite to 7 GPa and 873 K: Implications for the 410-km seismic discontinuity, *J. Geophys. Res.*, *106*, 30,575–30,591.

Litasov, K. D., E. Ohtani, and A. Sano (2006), Influence of water on major phase transitions in the Earth's mantle, in *Earth's Deep Water Cycle*, *Geophys. Monogr. Ser.*, vol. 168, edited by S. D. Jacobsen and S. van der Lee, pp. 95–111, AGU, Washington, D. C.

Liu, K. H. (2003), Effects of inelasticity on the apparent depth and detectability of seismic discontinuities in the mantle, *Geophys. Res. Lett.*, *30*(10), 1524, doi:10.1029/2003GL017059.

Martinez, W. L., and A. R. Martinez (2001), *Computational Statistics Handbook With MATLAB*, 1st ed., CRC Press, Boca Raton, Fla.

Park, J. (1996), Surface waves in layered anisotropic structures, *Geophys. J. Int.*, *126*, 173–184.

Priestly, K. F., J. Cipar, A. Egorkin, and N. I. Pavlenkova (1994), Upper-mantle velocity structure beneath the Siberian Platform, *Geophys. J. Int.*, *118*, 369–378.

Revenaugh, J., and S. A. Sipkin (1994), Mantle discontinuity structure beneath China, *J. Geophys. Res.*, *99*, 21,911–21,927.

Richard, G., D. Bercovici, and S. Karato (2006), Slab dehydration in the Earth's mantle transition zone, *Earth Planet. Sci. Lett.*, *251*, 156–167.

Ritsema, J., H. J. van Heijst, and J. H. Woodhouse (2004), Global transition zone tomography, *J. Geophys. Res.*, *109*, B02302, doi:10.1029/2003JB002610.

Saita, T., D. Suetsugu, T. Ohtaki, H. Takenaka, K. Kanjo, and I. Purwana (2002), Transition zone thickness beneath Indonesia as inferred using the receiver function method for data from the JISNET regional broadband seismic network, *Geophys. Res. Lett.*, *29*(7), 1115, doi:10.1029/2001GL013629.

Sambridge, M. (1999), Geophysical inversion with a neighbourhood algorithm—II, *Geophys. J. Int.*, *138*, 727–746.

Schmid, C., S. Goes, and S. van der Lee (2002), Fate of the Cenozoic Farallon slab from a comparison of kinematic thermal modeling with tomographics images, *Earth Planet. Sci. Lett.*, *204*, 17–32.

Shen, Y., and J. Blum (2003), Seismic evidence for accumulated oceanic crust above the 660-km discontinuity beneath southern Africa, *Geophys. Res. Lett.*, *30*(18), 1925, doi:10.1029/2003GL017991.

Silver, P. G., and W. W. Chan (1991), Shear wave splitting and subcontinental mantle, *J. Geophys. Res.*, *96*, 16,429–16,454.

Simmons, N. A., and H. Gurrola (2000), Multiple seismic discontinuities near the base of the transition zone in the Earth's mantle, *Nature*, *405*, 559–562.

Smyth, J. R., and D. J. Frost (2002), The effect of water on the 410-km discontinuity: An experimental study, *Geophys. Res. Lett.*, *29*(10), 1485, doi:10.1029/2001GL014418.

Solomatov, V. S., and D. J. Stevenson (1994), Can sharp seismic discontinuities be caused by non-equilibrium phase transformations?, *Earth Planet. Sci. Lett.*, *125*, 267–279.

Song, T. A., D. V. Helmberger, and S. P. Grand (2004), Low velocity zone atop the 410 seismic discontinuity in the northwestern United States, *Nature*, *427*, 530–533.

Suetsugu, D., T. Inoue, A. Yamada, D. Zhao, and A. Obayashi (2006), Towards mapping the three-dimensional distribution of water in the transition zone from P-velocity tomography and 660-km discontinuity depths, in *Earth's Deep Water Cycle*, *Geophys. Monogr. Ser.*, vol. 168, edited by S. D. Jacobsen and S. van der Lee, pp. 237–250, AGU, Washington, D. C.

van der Lee, S., H. Paulssen, and G. Nolet (1994), Variability of P660s phases as a consequence of topography of the 660 km discontinuity, *Phys. Earth Planet. Inter.*, *86*, 147–164.

Van der Meijde, M., F. Marone, D. Giardini, and S. Van der Lee (2003), Seismic evidence for water deep in Earth's upper mantle, *Science*, *300*, 1556–1558.

Vinnik, L. (1977), Detection of waves converted from P to SV in the mantle, *Phys. Earth Planet. Inter.*, *15*, 39–45.

Vinnik, L., M. Ravi Kumar, R. Kind, and V. Farra (2003), Super-deep low-velocity layer beneath the Arabian plate, *Geophys. Res. Lett.*, *30*(7), 1415, doi:10.1029/2002GL016590.

Vinnik, L. P., V. Farra, and R. Kind (2004), Deep structure of the Afro-Arabian hotspot by S receiver functions, *Geophys. Res. Lett.*, *31*, L11608, doi:10.1029/2004GL019574.

Wood, B. J. (1995), The effect of H_2O on the 410-kilometer seismic discontinuity, *Science*, *268*, 74–76.

Yuan, H., and K. Dueker (2003), Imaging the Cheyenne suture beneath the Laramie array in southeast Wyoming, *Eos Trans. AGU*, *84*(46), Fall Meet. Suppl., Abstract S11C-0316.

Yuan, H., and K. Dueker (2005), Teleseismic *P*-wave tomogram of the Yellowstone plume, *Geophys. Res. Lett.*, *32*, L07304, doi:10.1029/2004GL022056.

Yuan, H., K. Dueker, and D. Schutt (2006), Synoptic scale crustal thickness and velocity maps along the Yellowstone hotspot track, *Eos Trans. AGU*, *87*(52), Fall Meet. Suppl., Abstract S43A-1376.